

Rotating helical turbulence. Part I. Global evolution and spectral behavior

P.D. Mininni^{1,2} and A. Pouquet^{2,3}

¹*Departamento de Física, Facultad de Ciencias Exactas y Naturales, Universidad de Buenos Aires and CONICET, Ciudad Universitaria, 1428 Buenos Aires, Argentina.*

²*Computational and Information Systems Laboratory, NCAR, P.O. Box 3000, Boulder, Colorado 80307-3000, U.S.A.*

³*Earth and Sun Systems Laboratory, NCAR, P.O. Box 3000, Boulder, Colorado 80307-3000, U.S.A.*

(Dated: March 5, 2022)

We present results from two 1536^3 direct numerical simulations of rotating turbulence where both energy and helicity are injected into the flow by an external forcing. The dual cascade of energy and helicity towards smaller scales observed in isotropic and homogeneous turbulence is broken in the presence of rotation, with the development of an inverse cascade of energy now coexisting with direct cascades of energy and helicity. In the direct cascade range, the flux of helicity dominates over that of energy at low Rossby number. These cascades have several consequences for the statistics of the flow. The evolution of global quantities and of the energy and helicity spectra is studied, and comparisons with simulations at different Reynolds and Rossby numbers at lower resolution are done to identify scaling laws.

I. INTRODUCTION

Helicity, the alignment of velocity and vorticity, is a measure of the number of links in vorticity field lines, and an indication of lack of mirror-symmetry in a flow [1]. Isotropic and homogeneous turbulence with and without helicity has been thoroughly studied in the literature [2, 3, 4, 5]. Detailed comparisons using direct numerical simulations were carried up to large Reynolds numbers and spatial resolutions [6]. We can think about this problem following an analogy by Betchov [7]: a bag full of nails has after being shaken its nails pointing in every direction in space, and the resulting spatial distribution is mirror-symmetric. On the other hand, a well-shaken bag full of right-handed screws has its screws pointing in any direction, but the mirror-symmetry is broken by the screws. In isotropic and homogeneous turbulence, the presence of helicity does not change properties of turbulence such as the energy spectrum [3, 5, 8] or the energy decay rate [9]; both the energy and the helicity cascade towards smaller scales with the same time scales.

However, the presence of rotation breaks this degeneracy, as the dynamical equations for the flow evolution are now sensitive to mirror reflections. Rotation also breaks down the isotropy of the flow, introducing a preferred direction. The development of anisotropies in a rotating flow has been studied in great detail [10, 11, 12]. However, the role played by helicity in these flows has been given less attention with only a few exceptions [13, 14] even though the study of helical rotating flows is relevant for many atmospheric phenomena [15, 16, 17].

In a recent series of papers [18, 19], we presented evidence of differences in the scaling laws of rotating flows with and without helicity. The presence of helicity in a rotating flow changes the energy scaling, as shown in numerical simulations and explained with a phenomenological theory [19]. Changes in the directions of the energy and helicity cascades and their associated scaling laws have implications for the decay and predictability

of a helical rotating flow: helical rotating flows decay slower than non-helical rotating flows [20]. These differences imply that to model helical rotating flows in nature, subgrid models that take into account contributions to the turbulent transport coefficients from the helicity are required. In agreement with this, a sub-grid scale model based on the eddy-damped quasi-normal Markovian (EDQNM) closure [10, 21, 22] and that takes into account both the cascades of energy and of helicity, proved to behave better at reproducing simulations of rotating turbulence than models based solely on the energy cascade [23].

However, the grid resolution of these previous simulations of rotating helical turbulence (up to 512^3 grid points) was insufficient to study together and at sufficiently high Reynolds number the direct and inverse cascades; rather, these cascades were studied separately [19]. Also, the amount by which anisotropies develop at small scales (or the possible recovery of isotropy at small scale) was insufficiently quantified. In order to go further in our analysis of rotating turbulence, we present in this paper a detailed study of the results of two direct numerical simulations of rotating turbulence at unprecedented resolutions. The spatial resolution attained in the simulations allows us to confirm the scaling laws for the energy and helicity spectra predicted in [19] in runs where the direct and inverse cascades now coexist, each with well defined inertial ranges. We also analyze the evolution of global quantities in the simulations, the development of anisotropies in the flow, as well as scaling laws in the directions parallel and perpendicular to the axis of rotation. Section II describes the simulation and the numerical methods used, Sec. III describes the time evolution of global isotropic and anisotropic norms (energy, helicity, dissipation, characteristic length scales), and Sec. IV considers the energy and helicity spectra as well as their respective fluxes. We also compare with previous runs at different Rossby and Reynolds numbers in Sec. V to identify trends and dependencies with the controlling

parameters, the Reynolds and Rossby numbers. Finally, Sec. VI gives our conclusions.

In summary, the results presented in this paper provide a detailed description of the numerical simulations and compute global and spectral quantities often considered in previous studies of rotating turbulence. In a following paper (Paper II), we consider in detail the intermittency (or lack thereof) of the energy and helicity direct cascades, and study structure functions as well as probability density functions of velocity and helicity increments. Previous studies of rotating turbulence from numerical simulations [18, 24] showed a substantial decrease in the intermittency of the flow when rotation is strong (see also [25, 26, 27, 28] for experimental results). The present simulations can be used to quantify the impact of helicity in the flow intermittency, and the analysis presented in this first paper serves as a reference to allow comparisons between these large-resolution simulations and previous simulations of rotating turbulence in the literature. Overall, these studies allow us to consider the recovery of isotropy at small scales, as well as the development of structures at large and small scales in the flow, and give a thorough description of rotating turbulence at scale separations not considered before in direct numerical simulations.

II. NUMERICAL SIMULATIONS

We solve numerically the equations for an incompressible rotating fluid,

$$\frac{\partial \mathbf{u}}{\partial t} + \boldsymbol{\omega} \times \mathbf{u} + 2\boldsymbol{\Omega} \times \mathbf{u} = -\nabla \mathcal{P} + \nu \nabla^2 \mathbf{u} + \mathbf{F}, \quad (1)$$

and

$$\nabla \cdot \mathbf{u} = 0, \quad (2)$$

in a three dimensional box of size 2π with periodic boundary conditions using a parallel pseudospectral code with a spatial resolution of 1536^3 regularly spaced grid points (other resolutions will be briefly considered in Sec. V). Here \mathbf{u} is the velocity field, $\boldsymbol{\omega} = \nabla \times \mathbf{u}$ is the vorticity, and ν is the kinematic viscosity. The total pressure \mathcal{P} modified by the centrifugal term is obtained by taking the divergence of Eq. (1), using the incompressibility condition (2), and solving the resulting Poisson equation. We choose the rotation axis to be in the z direction: $\boldsymbol{\Omega} = \Omega \hat{z}$, with Ω the rotation frequency. Time derivatives are estimated using a second order Runge-Kutta method, and the code uses the 2/3-rule for dealiasing. As a result, the maximum wave number is $k_{\max} = N/3$ where N is the linear resolution. The code is fully parallelized with the message passing interface (MPI) library [29, 30].

The external mechanical forcing \mathbf{F} in Eq. (1) is given by a superposition of Arn'old-Beltrami-Childress (ABC)

flows [31],

$$\begin{aligned} \mathbf{F} = F_0 \sum_{k_F=k_1}^{k_2} \{ & [B \cos(k_F y) + C \sin(k_F z)] \hat{x} + \\ & + [C \cos(k_F z) + A \sin(k_F x)] \hat{y} + \\ & + [A \cos(k_F x) + B \sin(k_F y)] \hat{z} \}, \end{aligned} \quad (3)$$

where F_0 is the forcing amplitude, $A = 0.9$, $B = 1$, $C = 1.1$ [32]. An ABC flow, as e.g. in Eq. (3) for only one value of k_F , is an eigenfunction of the curl with eigenvalue k_F ; as a result, when used as a forcing function, it injects both energy and helicity in the flow. It should be noted that in homogeneous turbulence the helicity spectrum cannot develop if it is initially zero (see e.g., [10, 11]), or if an external mechanism does not inject helicity. In nature, helicity is created e.g., in the presence of rotation and stratification [33], or near solid boundaries in rotating vessels [34]. The use of the ABC forcing, although artificial, allows us to study helical rotating turbulence without the extra computational cost associated to the presence of boundaries or stratification.

Two simulations will be considered in Secs. III and IV, with the forcing acting from $k_1 = 7$ to $k_2 = 8$. This leaves some room in spectral space for cascades to develop both at large scale and at small scale. The viscosity is $\nu = 1.6 \times 10^{-4}$ in both runs, and the time step $\Delta t = 2.5 \times 10^{-4}$. For the first run (run A), $\Omega = 0.06$ and it is started from a flow initially at rest. The run was continued for near 10 turnover times, when a turbulent steady state was reached. The value of F_0 was such that in the steady state, the *r.m.s.* velocity $U = \langle u^2 \rangle^{1/2}$ was of order unity. For the second run (run B), $\Omega = 9$, and it is started from the velocity field in run A at $t \approx 10$. Run B was continued for 30 turnover times.

The Reynolds, Rossby, and Ekman numbers of the runs quoted in the following sections are defined as usual as:

$$\text{Re} = \frac{L_F U}{\nu}, \quad (4)$$

$$\text{Ro} = \frac{U}{2\Omega L_F}, \quad (5)$$

and

$$\text{Ek} = \frac{\text{Ro}}{\text{Re}} = \frac{\nu}{2\Omega L_F^2}, \quad (6)$$

where $L_F = 2\pi/\min\{k_F\}$, and the turnover time at the forcing scale is then defined as $T = L_F/U$.

In the following, it will be useful to also introduce a micro-Rossby number as the ratio of the *r.m.s.* vorticity to the background vorticity (rotation),

$$\text{Ro}_\omega = \frac{\omega}{2\Omega}. \quad (7)$$

The value of the micro-Rossby number plays a central role in the inhibition of the energy cascade in rotating

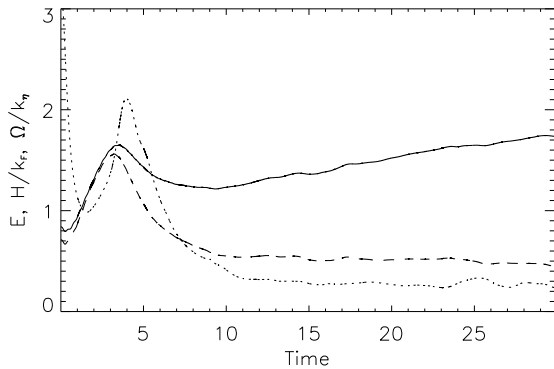


FIG. 1: Energy (solid), helicity normalized by the forcing wavenumber (dashed), and enstrophy rescaled by the dissipation wavenumber ≈ 500 (dotted) as a function of time in run B with $Ro = 0.06$.

turbulence [11]. If the micro-Rossby number is too small, non-linear interactions are completely damped. According to [35], anisotropies develop in rotating flows when the Rossby number $Ro \lesssim 1$ and when the micro-Rossby number $Ro_\omega \gtrsim 1$ (it is worth noting that the actual values for the transition depend on the particular flow studied).

Based on these definitions, the resulting Reynolds number for both runs was $Re \approx 5100$. The Rossby number of run A is $Ro \approx 8.5$, while the Rossby number of run B is $Ro \approx 0.06$. This results in Ekman numbers $Ek \approx 1.6 \times 10^{-3}$ for run A, and $Ek \approx 1.1 \times 10^{-5}$ for run B. The micro-Rossby number of run B is $Ro_\omega \approx 1.2$ (in all definitions, U and ω are measured in the steady state of run A, or when the inverse cascade of energy in run B starts). We therefore study flows with large Reynolds numbers, but with moderate Rossby numbers as often encountered in geophysical problems. Runs A and B will also be compared in Sec. V with other runs with helical forcing at lower resolution as already described in [19].

III. TIME EVOLUTION

A. Isotropic quantities

Figure 1 shows the time evolution of the energy, helicity, and enstrophy in run B. After a transient that lasts a few turnover times, energy grows monotonically in time. Helicity and enstrophy reach a steady state with nearly constant values, smaller than their values at $t = 0$ which correspond to the steady state in run A.

The enstrophy, proportional to the mean square vorticity, can be used as a proxy of the relevance of the rotation near the Taylor scale, as the ratio of the *r.m.s.* vorticity to the background rotation is proportional to the micro-Rossby number. However, turbulence is characterized by strong fluctuations of quantities in space and time, and one may ask how relevant is the background rotation in

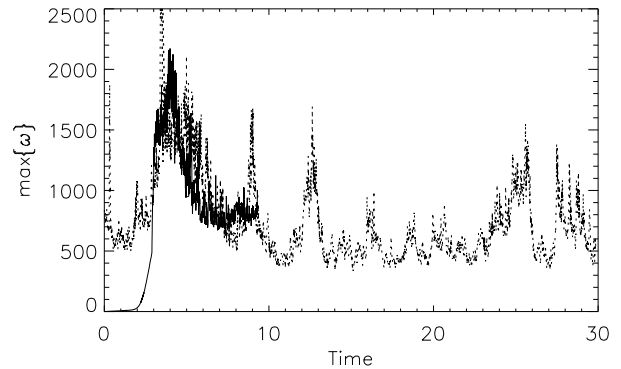


FIG. 2: Maximum vorticity in the flow as a function of time, for runs A (solid) and B (dotted).

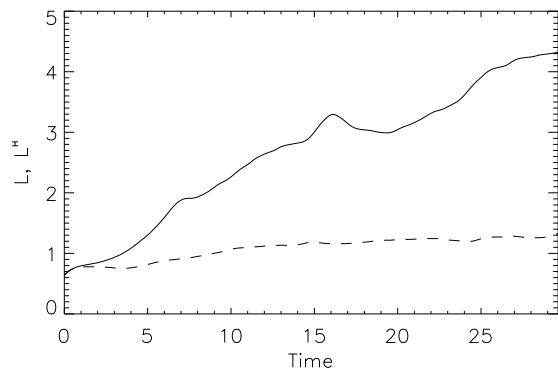


FIG. 3: Integral scales associated with the energy (solid line) and the helicity (dash line) as a function of time in run B.

the structures that correspond to these fluctuations. Another measure of the relevance of rotation at the small scales can thus be obtained by looking at regions in the flow with maximum vorticity. Fig. 2 shows the time history of the maximum of vorticity in runs A and B. In run A, which starts from a fluid at rest, $\max\{\omega\}$ grows rapidly from zero and after reaching a maximum saturates near ≈ 800 with strong fluctuations around the mean. In run B, started from the last snapshot of run A, $\max\{\omega\}$ starts from the previous value and reaches a maximum as the flow becomes anisotropic and the inverse cascade develops, and later saturates with a time average value of $\max\{\omega\} \approx 630$ with strong peaks. As a result, in run B $\max\{\omega\}/\Omega \approx 70$.

The increase of energy with time observed in Fig. 1 is associated to an inverse cascade of energy that results in an increase in the characteristic size of the energy-containing structures in the flow. This is illustrated in Fig. 3 by the time evolution of the isotropic integral

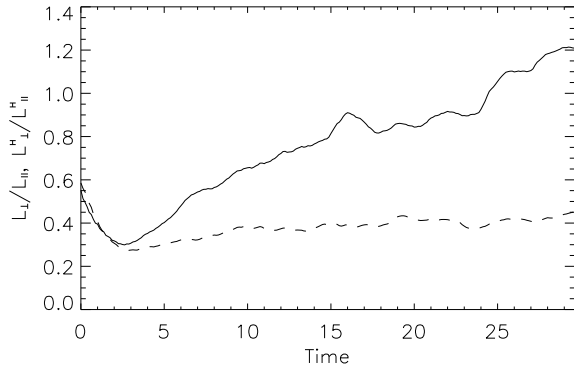


FIG. 4: Ratio of perpendicular to parallel integral scales, associated to the energy (solid) and to the helicity (dashed) as a function of time in run B.

scales of the energy

$$L = \frac{2\pi}{E} \sum_{k=1}^{k_{\max}} \frac{E(k)}{k}, \quad (8)$$

and of the helicity

$$L^H = \frac{2\pi}{H} \sum_{k=1}^{k_{\max}} \frac{H(k)}{k}, \quad (9)$$

where E and H are respectively the energy and the helicity, and $E(k)$ and $H(k)$ are the isotropic energy and helicity spectra. The wavenumber k corresponds to the mean radius of the spherical shell containing all modes with wave vectors with length between $k-0.5$ and $k+0.5$. Initially, both integral scales in run B are close to $L_F \approx 0.9$. However, as time evolves the integral scale of the energy increases, while the integral scale of the helicity remains approximately constant after a short transient increase.

B. The development of anisotropy

The flow in run B becomes anisotropic after a few turnover times. Several indicators can be defined to quantify the development of anisotropy. In this section, we will focus on global quantities, and later we will consider anisotropy from the point of view of Fourier spectra. Directional integral scales as in Eqs. (8) and (9) can be defined integrating spectra over wave vectors parallel and perpendicular to the rotation axis. We will consider the energy spectra $E(k_{\parallel})$ and $E(k_{\perp})$, where $E(k_{\parallel})$ is obtained by integrating the energy in all modes with wave vectors with $k_z = k_{\parallel}$ between $k_{\parallel}-0.5$ and $k_{\parallel}+0.5$ (i.e., integrating over planes in spectral space), and $E(k_{\perp})$ is obtained by integrating the energy in all modes with wave vectors with $(k_x^2 + k_y^2)^{1/2}$ between $k_{\perp}-0.5$ and $k_{\perp}+0.5$ (i.e., integrating in cylindrical shells; see e.g., [19, 36]). These spectra are often referred to in the literature as “reduced”

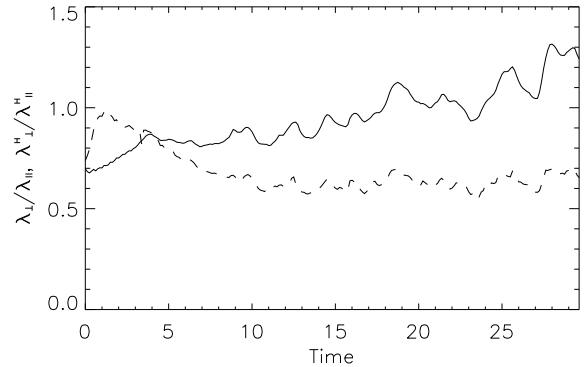


FIG. 5: Ratio of perpendicular to parallel Taylor scales, associated to the energy (solid) and to the helicity (dashed) as a function of time in run B at $Ro = 0.06$.

energy spectra. Similar procedures can be used to construct the reduced helicity spectra $H(k_{\parallel})$ and $H(k_{\perp})$. Then, following Eqs. (8) and (9), we define perpendicular and parallel integral scales

$$L_{\{\perp, \parallel\}} = 2\pi \frac{\sum_{k_{\{\perp, \parallel\}}=1}^{k_{\max}} k_{\{\perp, \parallel\}}^{-1} E(k_{\{\perp, \parallel\}})}{\sum_{k_{\{\perp, \parallel\}}=1}^{k_{\max}} E(k_{\{\perp, \parallel\}})} \quad (10)$$

$$L_{\{\perp, \parallel\}}^H = 2\pi \frac{\sum_{k_{\{\perp, \parallel\}}=1}^{k_{\max}} k_{\{\perp, \parallel\}}^{-1} H(k_{\{\perp, \parallel\}})}{\sum_{k_{\{\perp, \parallel\}}=1}^{k_{\max}} H(k_{\{\perp, \parallel\}})} \quad (11)$$

where the subindex $\{\perp, \parallel\}$ denotes that either parallel or perpendicular wave vectors are used.

Figure 4 shows the perpendicular-to-parallel ratio of integral scales for the energy and the helicity in run B. As Ω is suddenly increased at $t = 0$ from its previous value in run A, these two ratios first decrease from their initial values. Then, $L_{\perp}^H/L_{\parallel}^H$ increases slightly and seems to reach a steady state after $t \approx 10$, while L_{\perp}/L_{\parallel} keeps increasing monotonically in time on the whole, following the increase in the energy due to the inverse cascade. As a result, the energy (dominated by large scales) seems to become more anisotropic than the helicity which is concentrated in smaller scales.

Integral scales are dominated by the contributions from the energy containing scales. Note that both L and L^H are, after the short transient, larger than the forcing scale L_F (see Fig. 3). The ratios studied previously then give a global indication of anisotropies at scales that are in the inverse cascade range. Anisotropies in the (small scale) direct cascade range can be quantified, e.g., by the ratio of the perpendicular-to-parallel Taylor scales (Fig. 5). The perpendicular and parallel Taylor scales based on the energy and the helicity are defined as

$$\lambda_{\{\perp, \parallel\}} = 2\pi \left[\frac{\sum_{k_{\{\perp, \parallel\}}=1}^{k_{\max}} E(k_{\{\perp, \parallel\}})}{\sum_{k_{\{\perp, \parallel\}}=1}^{k_{\max}} k_{\{\perp, \parallel\}}^2 E(k_{\{\perp, \parallel\}})} \right]^{1/2}, \quad (12)$$

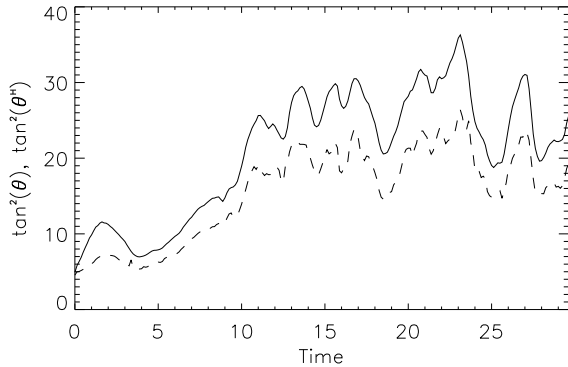


FIG. 6: Shebalin angles based on the energy (solid) and helicity spectra (dashed) as a function of time in run B.

$$\lambda_{\{\perp, \parallel\}}^H = 2\pi \left[\frac{\sum_{k_{\{\perp, \parallel\}}=1}^{k_{\max}} H(k_{\{\perp, \parallel\}})}{\sum_{k_{\{\perp, \parallel\}}=1}^{k_{\max}} k_{\{\perp, \parallel\}}^2 H(k_{\{\perp, \parallel\}})} \right]^{1/2}. \quad (13)$$

After a transient, the ratio $\lambda_{\perp}^H/\lambda_{\parallel}^H$ in Fig. 5 stabilizes at its original value at $t = 0$, while $\lambda_{\perp}/\lambda_{\parallel}$ increases with time. However, the increase in this ratio is slower than in the case of L_{\perp}/L_{\parallel} , and presents stronger fluctuations in time, being associated with scales in the inertial range of the direct energy and helicity cascades. Note that, at the onset of the inverse cascade for run B, the perpendicular Taylor scale is $\lambda_{\perp} \approx 0.25$, giving for the Taylor Reynolds number of that flow (based on the perpendicular scale), $R_{\lambda_{\perp}} = U\lambda_{\perp}/\nu \approx 1600$ (for run A, we have $R_{\lambda} \approx 900$ in the turbulent steady state; the increase of R_{λ} in run B is associated to the anisotropization and increase of characteristic scales of the flow when rotation is increased). Note that these values are larger than the values considered in experiments with similar Rossby numbers (see e.g., [25]).

Yet another measure of small scale spectral anisotropy is given by the Shebalin angles [37],

$$\tan^2(\theta) = 2 \frac{\sum_{k_{\perp}} k_{\perp}^2 E(k_{\perp})}{\sum_{k_{\parallel}} k_{\parallel}^2 E(k_{\parallel})}, \quad (14)$$

$$\tan^2(\theta^H) = 2 \frac{\sum_{k_{\perp}} k_{\perp}^2 H(k_{\perp})}{\sum_{k_{\parallel}} k_{\parallel}^2 H(k_{\parallel})}, \quad (15)$$

These angles measure the spectral anisotropy level, with the case $\tan^2(\theta) = 2$ corresponding to an isotropic flow. As the previous quantities, they only give a global measure of small-scale anisotropy, and are a byproduct of axisymmetric energy spectra (see [11, 22]). Figure 6 shows the time evolution of the angles based on the energy and on the helicity. The helicity at small scales is again more isotropic than the energy. However, unlike the previous quantities, the Shebalin angles grow fast and then

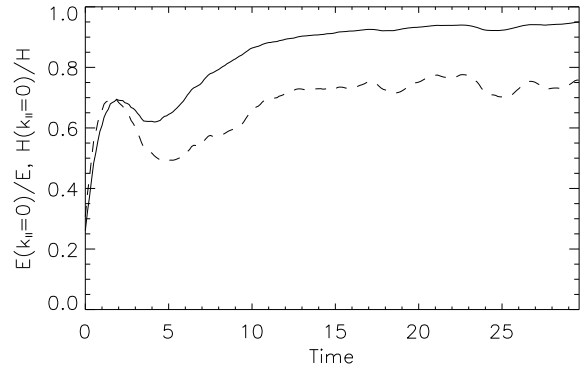


FIG. 7: Ratios $E(k_{\parallel} = 0)/E$ (solid line) and $H(k_{\parallel} = 0)/H$ (dash line) as a function of time in run B.

saturate in both cases, reaching a steady state after 10 turnover times.

Finally, the amount of energy and helicity in two-dimensional modes can be measured with the ratios $E(k_{\parallel} = 0)/E$ and $H(k_{\parallel} = 0)/H$ (see Fig. 7). Again, the spectral distribution of energy is more anisotropic than for helicity. Note that at late times a substantial fraction of the energy is in modes with $k_{\parallel} = 0$; at $t \approx 29$ near 95% of the energy is in those modes, while less than 75% of the helicity is in the same modes. All these results indicate that the distribution of energy is more anisotropic than that of helicity at all scales. As will be discussed next, this is due to the fact that helicity only suffers a direct cascade and is therefore transported in spectral space to smaller scales which are more isotropic.

IV. SPECTRAL BEHAVIOR

Figure 8 shows the isotropic energy and helicity spectra in run A. The run, with negligible rotation effects, displays the usual Kolmogorov scaling in the inertial range of the energy and the helicity, with a dual cascade of both quantities towards small scales. As in many simulations of three-dimensional isotropic and homogeneous turbulence, the short inertial range is followed by a bottleneck (which makes the spectra slightly shallower) and then by a dissipative range. The dual cascade towards smaller scales is further confirmed by examination of the energy and helicity fluxes (inset of Fig. 8) which are both positive and constant across the inertial range to the right of the forcing wavenumber. At wavenumbers smaller than k_F , both fluxes are negligible. The small amount of energy and helicity observed in the spectra at those wavenumbers is the result of backscatter, not of a cascade, and the energy in the large scales displays a slope compatible with a $\sim k^2$ scaling (see e.g., [38, 39]).

The energy and helicity spectra and fluxes at late times in run B at $Ro = 0.06$ are shown in Fig. 9. An inverse cascade of energy develops, as evidenced in the spectrum

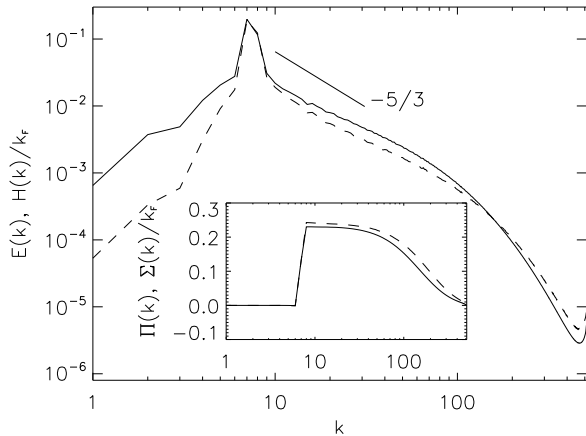


FIG. 8: Isotropic energy spectrum (solid) and helicity spectrum (dashed) normalized by the forcing wavenumber in run A with $Ro=8.5$. Kolmogorov scaling is shown as a reference. The inset gives the isotropic energy flux, and the helicity flux normalized by the forcing wavenumber.

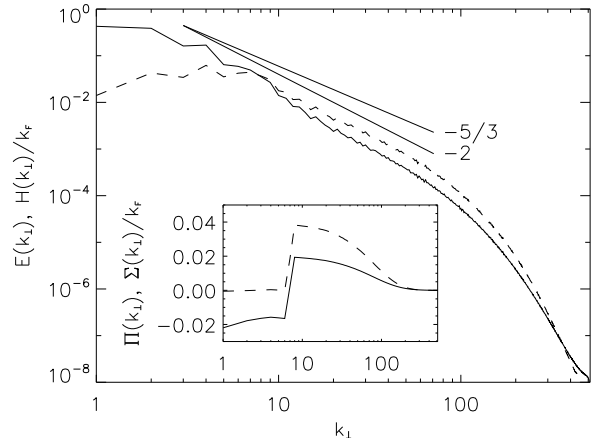


FIG. 10: Perpendicular energy and helicity spectra in run B with $Ro = 0.06$, with same labels as in Fig. 8. Kolmogorov and k^{-2} scaling laws are shown as a reference. The inset shows the perpendicular energy and helicity fluxes.

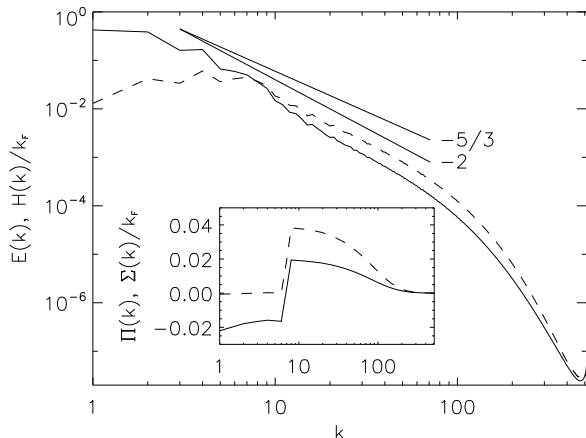


FIG. 9: Isotropic energy and helicity spectra in run B with $Ro = 0.06$ (same labels as in Fig. 8); $k^{-5/3}$ (Kolmogorov), and k^{-2} scaling laws are shown as a reference. The inset gives the isotropic energy and helicity fluxes. Note the excess of (normalized) helicity and of its flux in the small scales.

by the pile up of energy at scales larger than the forcing, and in the energy flux by a range of wavenumbers with nearly constant and negative transfer. However, unlike two-dimensional turbulence [40], not all the energy injected in the system undergoes an inverse cascade: a substantial fraction of the injected energy (approximately half at this Rossby number) is still transferred to small scales in a direct cascade of energy. Moreover, this direct cascade of energy is sub-dominant to a direct cascade of helicity. All the helicity injected in the system cascades to small scales, and as a result the helicity flux (properly adimensionalized) is larger than the energy flux at

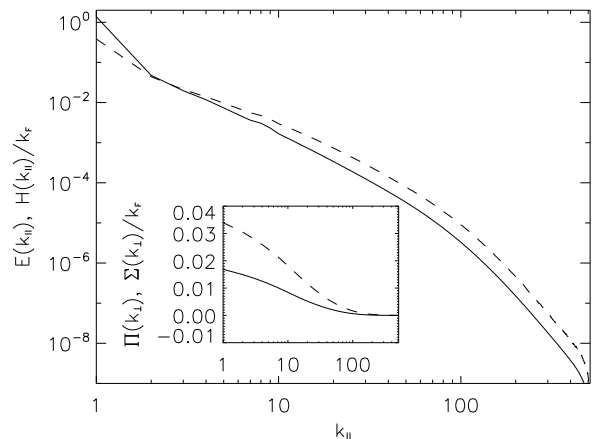


FIG. 11: Parallel energy and helicity spectra in run B, with same labels as in Fig. 8. The inset shows the parallel energy and helicity fluxes.

all wavenumbers larger than k_F .

Figure 10 displays the perpendicular energy and helicity spectra in run B at the same time as in Fig. 9. The same features as in the isotropic spectra can be identified, and almost no differences are observed between these spectra and the ones showed in Fig. 9. This is in agreement with the fact that at late times, $\approx 95\%$ of the energy and $\approx 75\%$ of the helicity are in modes with $k_{\parallel} = 0$ (i.e., wave vectors perpendicular to the axis of rotation). Here and in the isotropic case, the energy spectrum is slightly steeper than the helicity spectrum, the result of a dominant direct cascade of helicity.

No clear scaling is observed in the parallel spectra (Fig. 11). There is an excess of helicity at small scales when compared with the energy, as in the previous spectra, but

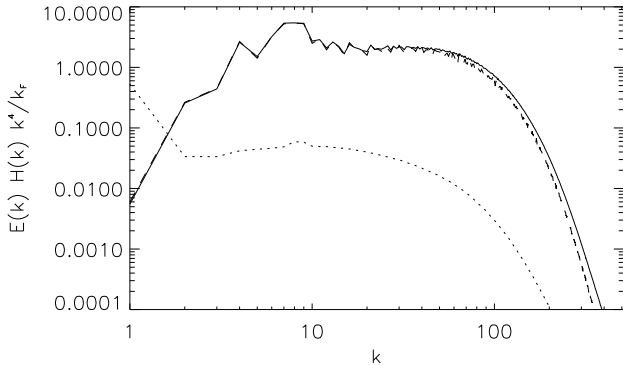


FIG. 12: Product of the energy and helicity spectra in run B, normalized by k_F and compensated by k^4 . The solid line corresponds to the isotropic spectra, the dash line to the perpendicular spectra, and the dotted line to the parallel spectra.

here an inertial range cannot be identified. Moreover, the energy and helicity fluxes in the parallel wave vectors are positive at all scales, and show no approximately constant range. The fluxes peak at $k_{\parallel} = 1$ and decrease fast for larger wavenumbers. This indicates that in the parallel direction, a small portion of the energy transferred towards large scales by the inverse cascade of energy in \mathbf{k}_{\perp} , is transferred back towards small scales although not through a cascade. The wavenumber band where forcing occurs is not identifiable either.

The presence of waves in a rotating flow slows down the direct energy cascade, resulting in a steeper energy spectrum than in isotropic and homogeneous turbulence. However, unlike isotropic and homogeneous turbulence, the slope of the energy spectrum depends on whether the flow is helical or not. This is the result of the flow developing, at small scales, a dominant direct cascade of energy in the former case, and a dominant direct cascade of helicity in the latter. In a flow with maximum helicity ($H(k) = kE(k)$), the energy and helicity spectra are, according to these arguments (see [19] for a detailed derivation), predicted to be $E \sim k_{\perp}^{-2.5}$ and $H \sim k_{\perp}^{-1.5}$. Note that this results in the relative helicity $H(k)/[kE(k)]$ independent of wavenumber, i.e. corresponding to an alignment of velocity and vorticity identical at all scales. In the general case (not maximally helical), the energy spectrum gets closer to a k_{\perp}^{-2} spectral law, but with both spectra such that their product is still $E(k)H(k) \sim k_{\perp}^{-4}$. The slope of the energy spectrum in the direct inertial range of Figs. 9 and 10 is ≈ 2.1 , while the slope of the helicity spectrum is ≈ 1.9 , in good agreement with these predictions (slopes were obtained through a least square fit). Figure 12 shows the product of all spectra compensated by k^4 . The isotropic and perpendicular spectra show a flat region compatible with this scaling, and the results are in good agreement with the arguments based on a dominant cascade of helicity in the helical rotating case. No clear scaling is observed in the parallel direction.

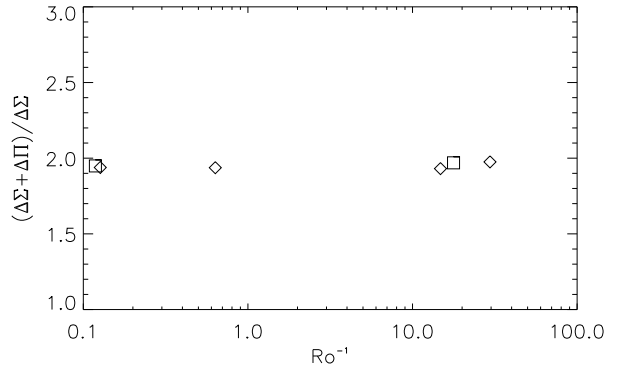


FIG. 13: Ratio $(\Delta\Sigma + \Delta\Pi)/\Delta\Sigma$ as a function of the inverse Rossby number for several runs (see text for definition). Squares correspond to runs A and B. Diamonds correspond to helical runs with 512^3 resolution, $k_F = 7$, and $Re \approx 1200$ for different Rossby numbers, as analyzed in [19].

V. SCALING WITH REYNOLDS AND ROSSBY NUMBERS

In this section we analyze an ensemble of runs in order to see the emergence of scaling laws when examining a range of Reynolds and Rossby numbers; to that effect, we combine runs A and B of this paper with previous simulations at different Reynolds and Rossby numbers [19]. The sub-dominant direct cascade of energy in run B is the result of the relation $\tilde{\epsilon} \sim k_F \epsilon$ at the forcing scale (where $\tilde{\epsilon}$ is the helicity injection rate dH/dt and ϵ the energy injection rate dE/dt), together with the development of an inverse cascade of energy at small enough Rossby number which removes some of the injected energy that would otherwise be available for the direct cascade. Since a fraction of the energy injected at k_F goes towards large scales (in run B, $|\Pi^-| \approx \epsilon/2$, where Π^- is the energy flux towards large scales, measured at wavenumbers smaller than k_F), while most of the helicity injected goes towards small scales (with Σ^+ the helicity flux towards small scales), the energy flux towards small scales Π^+ is smaller than Σ^+ in the entire direct cascade range (see e.g., Figs. 9 and 10). This results in a direct cascade dominated by the helicity, reminiscent of the pure direct cascade of helicity hypothesized in [41]. However, here the time scale of the direct cascade is affected by the presence of Rossby waves, resulting in the $E(k)H(k) \sim k_{\perp}^{-4}$ rule as discussed in [19].

This scenario is mainly based on two hypothesis, that the injection rates are related through $\tilde{\epsilon} \sim k_F \epsilon$ (with the proportionality constant equal to one when the forcing injects maximum helicity at only one wavenumber, and smaller than one when the forcing is not maximally helical), and that the ratio Σ^+/Π^+ in the direct cascade range increases with rotation (either monotonically or saturating at a small value of Ro such that the direct helicity flux becomes dominant).

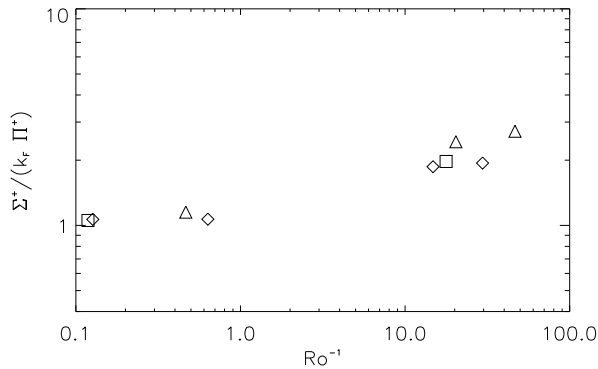


FIG. 14: Ratio $\Sigma^+/(k_F\Pi^+)$ as a function of the inverse Rossby number for several runs (see text for definitions). Squares correspond to runs A and B. Diamonds correspond to helical runs with 512^3 resolution, $k_F = 7$, and $\text{Re} \approx 1200$. Triangles correspond to helical runs with 512^3 resolution, $k_F = 2$, and $\text{Re} \approx 5700$ [19].

That the former condition holds, in the range of parameters tested in the present study, is illustrated in Fig. 13 which displays the normalized ratio $(\Delta\Sigma + \Delta\Pi)/\Delta\Sigma$ as a function of the Rossby number for several runs, where

$$\Delta\Sigma = (\Sigma^+ - \Sigma^-)/k_F = \tilde{\epsilon}/k_F ,$$

and

$$\Delta\Pi = \Pi^+ - \Pi^- = \epsilon .$$

Note that these differences (the amount of flux to small scales plus the amount of flux to large scales, since the latter is negative) are proportional to the helicity and energy injection rates $\tilde{\epsilon}$ and ϵ . For a forcing that injects maximum helicity, if $\tilde{\epsilon} = k_F\epsilon$, then $(\Delta\Sigma + \Delta\Pi)/\Delta\Sigma = 2$. The constancy of $(\Delta\Sigma + \Delta\Pi)/\Delta\Sigma$ for runs at different Reynolds and Rossby numbers, as observed in Fig. 13, builds confidence on the validity of the former hypothesis.

Figure 14 shows the ratio $\Sigma^+/(k_F\Pi^+)$, i.e., the ratio of energy flux towards small scales to the normalized helicity flux towards small scales, as a function of Ro^{-1} . While for large values of the Rossby number this ratio is close to unity (where a dual cascade of energy and helicity takes place, with both quantities having the same spectral index in the inertial range), as the Rossby number is decreased the ratio becomes larger than one. Simulations with very different Reynolds numbers and scale separation between the domain size and the forcing scale appear to collapse onto one curve that grows as Ro decreases, thus building confidence on the validity of the latter hypothesis.

VI. CONCLUSIONS

We presented results from two simulations of rotating turbulence at large Reynolds numbers and moderate

Rossby numbers, with spatial resolution of 1536^3 grid points and forced at intermediate scales, allowing for simultaneous direct and inverse cascades of the ideal invariants of the flow to develop. The forcing injects both energy and helicity, and both inverse and direct cascades of energy develop in the case of stronger rotation, together with a direct cascade of helicity. The inverse cascade range is dominated by the energy, and the flow is anisotropic and only weakly helical. On the other hand, in the direct cascade range, the normalized helicity flux is larger than the energy flux. The dominance of the helicity flux in this range results in the time scales of the direct cascade being imposed by the helicity. As a result, the small scale helicity spectrum is shallower than the energy spectrum. Both spectra scale as $E \approx k_{\perp}^{-e}$ and $H \approx k_{\perp}^{-h}$ with $e + h = 4$ as predicted by phenomenological arguments [19] (for the run with $\text{Ro} \approx 0.06$, it was found $e \approx 2.1$ and $h \approx 1.9$). The slope of the energy spectrum is slightly steeper than what is found in recent numerical simulations of non-helical rotating turbulence (see e.g. [18, 24]).

Comparisons with other simulations of helical rotating flows albeit at lower resolution allowed us to build confidence on the dominance of the direct cascade of helicity over the energy as the Rossby number is decreased. While direct and inverse inertial ranges of energy and helicity were identified in the isotropic and perpendicular spectra and fluxes, no clear scaling was found in the parallel direction. The energy and helicity fluxes in this direction are positive for all wavenumbers, and no range of scales with constant flux was found.

The development of anisotropies in the flow was studied using global and spectral quantities. In all cases, it was observed that the distribution of helicity is more isotropic than the distribution of energy. As an example, it was found that at late times $\approx 95\%$ of the energy is in modes with $k_{\parallel} = 0$, while less than 75% of the helicity is in the same modes (as a comparison, for run A $\approx 24\%$ of both the total energy and helicity are in modes with $k_{\parallel} = 0$). Other measures of anisotropy at both large and small scales gave consistent results. The vortical structures that develop in such flows and the anisotropy, as well as the recovery of isotropy at small scales, will be studied in more detail in Paper II using probability density functions of velocity and helicity increments, structure functions based on the symmetries of the problem and three-dimensional visualizations of the velocity and vorticity.

Acknowledgments

Computer time was provided by NCAR. NCAR is sponsored by the National Science Foundation. PDM acknowledges support from grant UBACYT X468/08 and PICT-2007-02211, and from the Carrera del Investigador Científico of CONICET.

-
- [1] H. K. Moffatt, “The degree of knottedness of tangled vortex lines,” *J. Fluid Mech.* **35**, 117(1969).
- [2] V. Borue and S. A. Orszag, “Spectra in helical three-dimensional homogeneous isotropic turbulence,” *Phys. Rev. E* **55**, 7005 (1997).
- [3] Q. Chen, S. Chen, and G. L. Eyink, “The joint cascade of energy and helicity in three-dimensional turbulence,” *Phys. Fluids* **15**, 361 (2003).
- [4] Q. Chen, S. Chen, G. L. Eyink, and D. D. Holm, “Intermittency in the joint cascade of energy and helicity,” *Phys. Rev. Lett.* **90**, 214503 (2003).
- [5] D. O. Gómez and P. D. Mininni, “Understanding turbulence through numerical simulations,” *Physica A* **342**, 69 (2004).
- [6] P. D. Mininni, A. Alexakis, and A. Pouquet, “Large-scale flow effects, energy transfer, and self-similarity on turbulence,” *Phys. Rev. E* **74**, 016303 (2006).
- [7] R. Betchov, “Semi-isotropic turbulence and helicoidal flows,” *Phys. Fluids* **4**, 925 (1961).
- [8] R. H. Kraichnan, “Helical turbulence and absolute equilibrium,” *J. Fluid Mech.* **59**, 745 (1973).
- [9] M. Lesieur, *Turbulence in fluids* (Kluwer Acad. Press, Dordrecht, 1997).
- [10] C. Cambon and L. Jacquin, “Spectral approach to non-isotropic turbulence subjected to rotation,” *J. Fluid Mech.* **202**, 295 (1989).
- [11] C. Cambon, N. N. Mansour, and F. S. Godeferd, “Energy transfer in rotating turbulence,” *J. Fluid Mech.* **337**, 303 (1997).
- [12] F. Waleffe, “Inertial transfers in the helical decomposition,” *Phys. Fluids A* **5**, 677 (1993).
- [13] S. Galtier, “Weak inertial-wave turbulence theory,” *Phys. Rev. E* **68**, 015301 (2003).
- [14] Y. Morinishi, K. Nakabayashi, and S. Ren, “Effects of helicity and system rotation on decaying homogeneous turbulence,” *Japan Soc. Mech. Eng. Series B* **44**, 410 (2001).
- [15] B. W. Kerr and G. L. Darkow, “Storm-relative winds and helicity in the tornadic thunderstorm environment,” *Weath. and Forecast.* **11**, 489 (1996).
- [16] D. K. Lilly, “The structure, energetics, and propagation of rotating convective storms. Part II: helicity and storm stabilization,” *J. Atmosph. Sc.* **43**, 126 (1988).
- [17] P. M. Markowski, J. M. Straka, E. N. Rasmussen, and D. O. Blanchard, “Variability of storm-relative helicity during VORTEX,” *Mont. Weath. Rev.* **126**, 2959 (1998).
- [18] P. D. Mininni, A. Alexakis, and A. Pouquet, “Scale interactions and scaling laws in rotating flows at moderate Rossby numbers and large Reynolds numbers,” *Phys. Fluids* **21**, 015108 (2009).
- [19] P. D. Mininni and A. Pouquet, “Helicity cascades in rotating turbulence,” *Phys. Rev. E* **79**, 026304 (2009).
- [20] T. Teitelbaum and P. D. Mininni, “Effect of helicity and rotation on the free decay of turbulent flows,” *Phys. Rev. Lett.* **103**, 014501 (2009).
- [21] S. A. Orszag, “Statistical theory of turbulence,” in *Fluid dynamics, Les Houches 1973*, pp. 237–374, R. Balian and J. L. Peube, eds. (Gordon and Breach, New York, 1977),
- [22] F. Bellet, F. S. Godeferd, and F. S. Scott, “Wave turbulence in rapidly rotating flows,” *J. Fluid Mech.* **562**, 83 (2006).
- [23] J. Baerenzung, P. D. Mininni, A. Pouquet, H. Politano, and Y. Ponty, “Spectral modeling of rotating turbulent flows,” arXiv:0812.1821 (2008).
- [24] W.-C. Müller and M. Thiele, “Scaling and energy transfer in rotating turbulence,” *Europhys. Lett.* **77**, 34003 (2007).
- [25] C. N. Baroud, B. B. Plapp, Z.-S. She, and H. L. Swinney, “Anomalous self-similarity in a turbulent rapidly rotating fluid,” *Phys. Rev. Lett.* **88**, 114501 (2002).
- [26] C. N. Baroud, B. B. Plapp, H. L. Swinney, and Z.-S. She, “Scaling in three-dimensional and quasi-two-dimensional rotating turbulent flows,” *Phys. Fluids* **15**, 2091 (2003).
- [27] P. Sagaut and C. Cambon, *Homogeneous turbulence dynamics* (Cambridge Univ. Press, Cambridge, 2008).
- [28] C. Simand, F. Chillà, and J.-F. Pinton, “Study of inhomogeneous turbulence in the closed flow between corotating disks,” *Europhys. Lett.* **49**, 336 (2000).
- [29] D. O. Gómez, P. D. Mininni, and P. Dmitruk, “MHD simulations and astrophysical applications,” *Adv. Sp. Res.* **35**, 899 (2005).
- [30] D. O. Gómez, P. D. Mininni, and P. Dmitruk, “Parallel simulations in turbulent MHD,” *Phys. Scripta* **T116**, 123 (2005).
- [31] S. Childress and A. D. Gilbert, *Stretch, twist, fold: the fast dynamo* (Springer-Verlag, Berlin, 1995).
- [32] V. Archontis, S. B. F. Dorch, and A. Nordlund, “Dynamo action in turbulent flows,” *Astron. Astrophys.* **410**, 759 (2003.)
- [33] H. K. Moffatt, *Magnetic field generation in electrically conducting fluids* (Cambridge Univ. Press, Cambridge, 1978).
- [34] F. S. Godeferd and L. Lollini, “Direct numerical simulations of turbulence with confinement and rotation,” *J. Fluid Mech.* **393**, 257 (1999).
- [35] L. Jacquin, O. Leuchter, C. Cambon, and J. Mathieu, “Homogeneous turbulence in the presence of rotation,” *J. Fluid Mech.* **220**, 1 (1990).
- [36] A. Alexakis, B. Bigot, H. Politano, and S. Galtier, “Anisotropic fluxes and nonlocal interactions in magnetohydrodynamic turbulence,” *Phys. Rev. E* **76**, 056313 (2007).
- [37] J. V. Shebalin, W. H. Matthaeus, and D. Montgomery, “Anisotropy in MHD turbulence due to a mean magnetic field,” *J. Plasma Phys.* **29**, 525 (1983).
- [38] P. A. Davidson, *Turbulence: an introduction for scientists and engineers* (Oxford Univ. Press, Oxford, 2004).
- [39] P. G. Saffman, “The large-scale structure of homogeneous turbulence,” *J. Fluid Mech.* **27**, 581 (1967).
- [40] G. Boffetta, “Energy and enstrophy fluxes in the double cascade of two-dimensional turbulence,” *J. Fluid Mech.* **589**, 253 (2007).
- [41] A. Brissaud, U. Frisch, J. Léorat, M. Lesieur, and A. Mazure, “Helicity cascades in fully developed isotropic turbulence,” *Phys. Fluids* **16**, 1366 (1973).